A Tribo-Multibody Model for valve train kinematic analysis, quasi-statics of lubricated contact and assessment of structural integrity

M. Kushwaha* BEng
H. Rahnejat* BSc,MSc,PhD,DIC,CEng,MIMechE,FCybS
P.M. Johns-Rahnejat** BSc MSc PhD DIC
* Department of Mechanical Engineering, University of Bradford, Bradford BD7 1DP,U.K.
** First Dynamics Ltd., 3 Alexandra Crescent, Ilkley, West Yorkshire LS29 9ER, U.K.

Abstract

This paper presents a generic multi-body model of a vehicular valve train for cam and flat follower arrangement. The model is created in ADAMS and is fully parameterised and customised. It incorporates all the inertial members, the constraint functions, and the sources of compliance in the valve train. The latter includes the valve train spring characteristics, as well as the contact compliance between the cam and the flat follower. The contact domain is treated as a counterformal concentrated lubricated region, subjected to elastohydrodynamic regime of lubrication (EHL). The prevailing contact geometry is one of finite line contact. Elastohydrodynamic (EHD) formulation is carried out to obtain the solution for the contact pressure distribution and the elastic lubricant film shape, for both steady state entraining motion as well as transient combined rolling and squeeze film motion. An extrapolated lubricated contact load equation is found through a full combinatorial Design of Experiments (DOE) and linear and non-linear regression analyses. This equation is employed to obtain the instantaneous contact load in the lubricated conjunction for pure entraining motion. A two dimensional stress module evaluates the sub-surface stresses, that are largely responsible for failure of contacting bodies due to fatigue spalling.

1. Introduction

The contact between cam and the follower is responsible for a sizeable proportion of the frictional losses experienced in the internal combustion engines [1,2].A progressive demand for increasing engine speeds in modern motor vehicles, and in particular in racing vehicles have resulted in the valve train performance becoming a critical factor. Faster valve accelerations are, therefore, desired which can lead to increases in inertial imbalances, thus rendering high levels of Noise, Vibration and Harshness (NVH) [3,4].

Difficulties also exist in the formation of coherent lubrication in the contact conjunction between the cam and the follower [5,6]. Indeed under steady state conditions theoretical analyses point to the loss of a lubricant film in the vicinity and immediately prior to the cam nose to follower contact [7,8]. This problem is further exacerbated at cold start and at low engine speeds due to high frictional torques and/or thin film thicknesses. In fact it is claimed, through theoretical investigations, that in the aforementioned regions the predominant regime of lubrication is due to boundary films [5]. However, experimental evidence obtained by Hamilton [5] does not concur with the theoretical findings. Until recently the presence of a lubricant film measured in these regions could not be explained using the theory of elastohydrodynamic lubrication (EHL). Solutions obtained for transient EHL conditions point to a combined entraining and squeeze film action [7,9,10]. These solutions indicate the critical role that the squeeze film action plays in the retention of a lubricant film, where the contribution due to rolling is insignificant (either because of low entraining speeds or a reversal in the position of inlet boundary near the cam nose). The effect of the squeeze film action is particularly significant at the start up and low engine speeds. Furthermore, its contribution is enhanced by

the presence of trapped lubricant in the surface undulations formed by asperities. Therefore, the absence of wear is much owed to the combined effects of squeeze film motion and local trapped films.

The failure of the rolling surfaces is not only caused by the long process of wear, but also by fatigue spalling due to the generation of unacceptable sub-surface stresses caused by high lubricant pressures in the elastohydrodynamic conjunction [11,12,13]. Therefore, the mechanical properties of materials for cam and followers, as well as the lubricant pressures and dynamic loads are important in the design of cam/follower pairs.

It is clear that design of new valve trains is critically affected by the cam and follower contact conditions. The trend for the future development of internal combustion engines is to increase valve accelerations, whilst minimising NVH effects. This points to a reduction in the mass of the inertial members (i.e. using lighter cams and followers and their attachments), thereby reducing the valve spring rate. However, lighter materials point to a reduced fatigue strength of contacting members. A compromise approach is, therefore, the key for future developments to come. An integrated approach incorporating both the NVH aspects of the valve train and component structural integrity assessment is seen as essential. This approach calls for in-depth analysis of the problem, one that unfortunately has been neglected for too long.

This paper highlights a detailed methodology to remedy this situation.

2. The Multi-body Model

The multi-body dynamic model of the system is a lumped parameter model that consists of the inertial components of the system referred to as "parts". The parts are constrained to move with respect to one another in a specified manner, thus renderring the ideal functions that are desired in the valve train system. The aim of the multi-body model is to incorporate the "parts" and the system constraints, as well as including the sources of system compliance. The overall model, therefore, can be used for a non-linear dynamic analysis of the system in order to investigate its NVH performance. Below we describe the constituent elements of the model, before proceeding to the formulation of the problem.

2.1 Inertial Parts

Table 1 provides a list of parts that are included in the multi-body valve train model. The first column in the table lists the names of rigid parts and the second column gives the masses of each part. Figure 1 also shows the arrangement of parts in the overall valve train model.

2.2 Constraints

Parts in the multi-body model are constrained to one another by rigid constraints as described above. These constraints are applied at given geometric locations between parts. These locations are referred to as "markers". Table 2 lists named joined parts in the first two columns, followed by the type of joint employed, and the co-ordinated location of the joints with respect to the model's global frame of reference shown in figure 1. Each joint includes a number of constraints that are represented by scalar algebraic constraint functions. These functions are non-linear algebraic equations. The number of constraints imposed by each formulated joint type is given in the key to table 2. The description of the constraint functions are provided in section 4.

Note that it is assumed that no separation and tappet spin can occur in the rolling contact of the cam-follower pair. However, in the real situation such motions can take place under dynamic conditions.

2.3 Sources of Compliance

The sources of compliance in a real valve train are manifold. This includes the valve train spring stiffness and damping (the latter ignored in the model), the contact compliance in the lubricated conjunction between the cam and follower described in section 2.4, the contact compliance between the valve stem and the valve seat (also ignored in the model due to its complexity- this requires a separate detailed analysis), the tangential traction in the contact domain which is also omitted in the current analysis. The spring stiffness is 38 N/mm.

2.4 Cam-Tappet Concentrated Contact

The cam to flat follower contact at a particular cam angle can be regarded to be the same as the contact that a roller of the same radius as the cam instantaneous radius makes with a flat. The dry contact of such a roller on a flat is now well understood and follows the Hertzian stress analysis of a roller indenting a semi-infinite elastic half-space. The Hertzian theory assumes that the surfaces of the roller and the plane are perfectly frictionless and hence the generated reaction forces are normal to the plane of contact. When the two bodies are elastic, the contact length is assumed to be slightly shorter than the roller length and the strains that are applied remain within the elastic limit. The contact width is necessarily small in comparison to the principal radii of curvature of the bodies, in this case the instantaneous cam radius.

Using the Hertzian theory, the deflections under the induced contact pressure at any point in the contact region can be obtained as:

$$\delta(x,y) = [\frac{(1-\nu_1^2)}{\pi E_1} + \frac{(1-\nu_2^2)}{\pi E_2}] \iint_{x_1 y_1} \frac{p(x,y)}{\sqrt{(x-x_1)^2 + (y-y_1)^2}} dx_1 dy_1 \qquad (1)$$

The pressure distribution is assumed to be elliptical in the transverse direction for dry contacts following the Hertzian theory. This of course is not the case for lubricated contact under EHL condition. However, the EHL pressure distribution follows closely the Hertzian pressure profile closely except for the inlet trail and the exit secondary pressure peak. The conformity to the Hertzian conditions is further emphasised with thin films and starved inlets, a feature of cam/follower contact. Therefore, for all intent and purposes the contact deformation can be obtained from the Hertzian pressure distribution. This makes the evaluation of the central deflection quite simple by analytic means. Hence, such an analytic expression can be included in a multi-body model in order to determine the contact deformation under load and the corresponding contact width, eliminating the need to solve the elasticity problem in each time step of the transient contact dynamics. The EHL solution highlighted below also yields the extrapolated film thickness equation that can be used to determine the film thickness at the same localities. Hence the transient tribo-dynamic problem becomes more manageable in each step of time.

Assuming the lateral Hertzian elliptical pressure profile and that the pressure and the footprint half-width at any section are proportional to their respective values at the contact centre [14], then: (see figure 2)

$$\frac{b_1}{p_1} = \frac{b_0}{p_0} = \frac{D}{4E} \tag{2}$$

The central contact half-width and the corresponding pressure can be obtained from the classical Hertzian theory as:

$$b_o^2 = \frac{2}{\pi}[\frac{(1-\nu_1^2)}{E_1} + \frac{(1-\nu_2^2)}{E_2}]\frac{WD}{L} \tag{3}$$

$$p_o = \frac{2W}{\pi b_o L} \tag{4}$$

The lateral elliptical pressure profile in any cross-section of the overall pressure distribution is given by: (see figure 2)

$$p(x_1, y_1) = p_1[1 - (\frac{x_1}{b_1})^2]^{1/2} \tag{5}$$

Substituting from equation (5) into equation (1), and integrating over the contact domain as shown in figure 2, the deflection at point (x,y) can be obtained. This procedure can be carried out for all points within the contact domain. For the central contact point (i.e. x=y=0):

$$\delta(0,0) = b_0 p_0[\frac{1-\nu_1^2}{E_1} + \frac{1-\nu_2^2}{E_2}](\ln\frac{4b}{b_0} + 0.5) \tag{6}$$

The load deflection characteristics of the contact in terms of the central deflection can be obtained by replacing in equation (6) from equations (3) and (4). This would indicate the non-linearity of the contact compliance. It should also be observed that the contact compliance alters with the instantaneous contact radius of the cam. Such variation of the contact stiffness itself is responsible for high frequency contents in the valve train spectrum, a fact that is largely ignored by most of the reported models. It should be noted that valve train spectra, for example in the case of 6 cylinder in-line engines contain significant contributions at $1\frac{1}{2}$ engine order and its multiples [3,4], the higher harmonics of which can easily coincide with the local elastic deformation response frequency, usually in the region of 100-300 Hz for line contact conditions as reported by Rahnejat [9,15].

The above analysis, whilst useful in the analytic evaluation of the contact deformation and dimensions, is based upon the assumption of an axial uniform pressure distribution. This assumption yields a rectangular footprint which deviates from reality, where the footprint shape has been shown to approximate to a "dog-bone" shape [16]. To obtain the film thickness and the correct pressure distribution a solution to finite line EHL is required.

3. Formulation of Elastohydrodynamic Conjunction

The lubricated contact pressure distribution occurs axially along the depth of cam, and laterally along the direction of entraining motion, with the contact half-widths in all cross-sections being much smaller than the contact length. This gives rise to a line contact condition of finite length. Therefore, a finite line EHL solution is sought. For this purpose the simultaneous solution of

the Reynolds' hydrodynamic equation and the elastic film shape is necessary. Solutions for finite line contact EHL problem have been attempted to a much lesser extent than those for elliptical point contact conditions. The main solutions have been by Mostofi [17], Mostofi and Gohar [10], and Rahnejat [9]. The work in reference [9] includes the effect of squeeze film action. The other solution is reported by Dowson, Taylor and Zhu [7] for the case of cam-follower contact. This paper follows the same general finite line solution methodology reported in reference [9] for the case of combined entraining and squeeze film action.

3.1 Reynolds' Equation

For the velocity induced flow in the transverse contact direction, y (see figure 3), subjected to normal approach of mating rolling members, the Reynolds' equation is:

$$\frac{\partial}{\partial x}[\frac{\rho h^3}{\eta}\frac{\partial p}{\partial x}]+\frac{\partial}{\partial y}[\frac{\rho h^3}{\eta}\frac{\partial p}{\partial y}]=12\{u\frac{\partial(\rho h)}{\partial y}+w_s\} \tag{7}$$

Using the method of reduced pressures [9,17] the following relationship results:

$$q=\frac{1}{\alpha}(1-e^{-\alpha p}) \tag{8}$$

Now the dimensionless groups provided in the nomenclature can be employed to non-dimensionalise the Reynolds' equation in terms of the reduced pressures as:

$$\frac{\partial}{\partial \bar{x}}[\bar{\rho}h^{*3}\frac{\partial q^*}{\partial \bar{x}}]+\frac{\partial}{\partial \bar{y}}[\bar{\rho}h^{*3}\frac{\partial q^*}{\partial \bar{y}}]=12\{u^*\frac{\partial(\bar{\rho}h^*)}{\partial \bar{y}}+w_s^*\} \tag{9}$$

The variation of density with lubricant pressure is obtained from Dowson and Higginson [18] as:

$$\bar{\rho}=\frac{1+0.6P^*}{1+1.7P^*} \tag{10}$$

3.2 Elastic Film Shape

The EHL film thickness can be written in dimensionless form as [9,10,19]:

$$h^*(\bar{x},\bar{y})=\{\bar{p}_r(\bar{x},\bar{y})-[\bar{\delta}(0,0)-\bar{\delta}(\bar{x},\bar{y})]\}+h_0^* \tag{11}$$

The term $\bar{p}_r(\bar{x},\bar{y})$ is the separation of the bodies in their undeformed state (i.e. the cam profile in this case). The term in the square brackets is referred to as the elastic film shape, and h_0^* is the dimensionless central oil film thickness.

It should be noted that the profile of the cam varies along the direction of entraining motion, $\bar{y}$ and is flat in the transverse direction, $\bar{x}$. Therefore:

$$\bar{p}_r(\bar{x},\bar{y})=\frac{\bar{y}^2}{2} \tag{12}$$

The elastic film shape components in equation (11) are obtained from equation (1) and put in the dimensionless form as:

$$\bar{\delta}(\bar{x},\bar{y}) = \frac{\delta(x,y)}{R} \tag{13}$$

where R is the instantaneous reduced radius of the counterformal contact.

3.3 Discretisation of the Reynolds' Equation

In order to solve the EHL of finite line problem, it is necessary to discretise the Reynolds' equation. It should be noted that the pressure gradient in the vicinity and prior to the exit constriction assumes a large positive gradient in order to achieve the lubricant flow continuity. Immediately after the exit constriction the lubricant assumes pressures that are at or below the atmospheric condition. This results in a corresponding large negative pressure gradient. The situation at the inlet is not as dramatic but results in large changes in lubricant film thickness, density and dynamic viscosity. Therefore, large variations of pressures and corresponding film thicknesses makes the simultaneous solution of the Reynolds' and elastic film shape equations subject to many iterations, when represented in the form given by equation (9). To alleviate this problem the following substitution is employed, providing smoother rates of change in the Reynolds' equation:

$$\phi = q^* h^{*3/2} \tag{14}$$

Substituting this into equation (9), we get:

$$h^{*3/2}\left[\frac{\partial}{\partial \bar{x}}\left(\bar{\rho}\frac{\partial \phi}{\partial \bar{x}}\right) + \frac{\partial}{\partial \bar{y}}\left(\bar{\rho}\frac{\partial q\phi}{\partial \bar{y}}\right)\right] - \frac{3}{2}\phi\left[\frac{\partial}{\partial \bar{x}}\left(\bar{\rho}h^{*1/2}\frac{\partial h^*}{\partial \bar{x}}\right) + \frac{\partial}{\partial \bar{y}}\left(\bar{\rho}h^{*1/2}\frac{\partial h^*}{\partial \bar{y}}\right)\right] = 12\left\{u^*\frac{\partial(\bar{\rho}h^*)}{\partial \bar{y}} + \bar{\rho}w_s^*\right\} \tag{15}$$

This equation can now be written in finite difference form. In order to do so a mesh must be constructed. Aside from the high pressures generated at the exit constriction along the direction of entraining motion described above, edge stress discontinuities also occur in the axial contact direction owing to the unprofiled lateral shape of the cam. These edge stress discontinuities result in side constrictions; yielding thin lubricant films and high pressure spikes. It is, therefore, necessary to construct irregular meshes in order to introduce more computation elements within the regions of high pressure gradients [9,14,17,20].

In this analysis an irregular mesh is constructed as shown in figure 3. Note the "dog-bone" shape of the contact. The mesh has regular elements in the direction of entraining motion and irregular spacing in the lateral direction of the cam, based on an arithmetic progression that increases the number of elements in the regions of side constriction. The same approach is highlighted in references [9,17]. Now using finite central difference technique, the Reynolds' equation (15) can be discretised as:

$$R_{i,j}\phi_{i,j} + L_{i,j}\phi_{i-1,j} + A_{i,j}\phi_{i,j+1} + B_{i,j}\phi_{i,j-1} - C_{i,j}\phi_{i,j} - S_{i,j} = 0 \tag{16}$$

where R, L, A, and B refer to the coefficients applied to the neighbouring terms to the right, left, above and below the central term. C is the coefficient of the central term, and S is the right hand side term of the Reynolds' equation referred to as the source term. These terms in equation (16) can be obtained from reference [17].

Equation (16) is highly non-linear, the solution to which is obtained in an iterative process, using over-relaxation for rapid convergence. The solution methodology is similar to that described in references [10,17]. The difference in this solution is the inclusion of squeeze film action, as also reported in reference [9].

3.4 EHL Results

Referring to figure 3, the various cross-sections in the direction of entraining motion and in the transverse direction are shown in this guide contour for a symmetrical contact about the section 1-1. The mid-point A along the section 1-1 corresponds to the central oil film thickness, h_0^* in equation (11). Point B along the same section corresponds to the rear exit film. Section 5-5 is through the side constriction in the direction of entraining motion. The other sections; 3-3, 2-2, and 4-4 are in the axial direction, perpendicular to the direction of entraining motion. Section 3-3 is through the centre of the contact, whilst section 2-2 corresponds to the leading edge of the Hertzian region. Section 4-4 is through the rear exit in the longitudinal direction. The intersection of sections 4-4 and 5-5, depicted by point C, define the side constriction region, having the thinnest lubricant thickness under flooded or symmetrically starved conditions.

Figure 4(a) shows the pressure profiles along section 3-3 for two different values of squeeze velocity, with all other governing parameters remaining constant. The pressure profile for pure entraining motion, taken from reference [17] is also depicted in the figure. It can be observed that the secondary pressure peak tends to the centre of the contact, as expected. It should be noted that at pure squeeze conditions the secondary pressure peak merges with the primary peak and occurs along the section 3-3. Figure 4(b) illustrates the corresponding film shapes along the same section. Increasing the squeeze velocity increases the film thickness under the same load. This indicates an increased load contact carrying capacity under combined rolling and normal approach, a fact that is clearly responsible for survival of machine elements under much of the transient conditions that occur in start up and low speeds of entraining motion.

The longitudinal pressure profiles and film shapes for the same conditions for sections 3-3 and 4-4 are shown in figures 5 and 6. The corresponding pressures under pure entraining motion and under dry elastostatic conditions are taken from reference [17]. Along the section 3-3 the changes are marginal with an increase in the squeeze velocity. The effect of squeeze film action is more pronounced along the exit pressure profiles, particularly in the vicinity of the end closure films corresponding to the position of point C in figure 3. In lubricated contacts the central pressures are reduced from their elastostatic levels as anticipated. The edge stresses at contact extremeties, however, increase under lubricated conditions, and particularly with an increase in the squeeze velocity. In practice the lubricant supply at low pressures on the shoulders of the contact and immediately adjacent to the Hertzian region undergo a positive pressure gradient due to an inward flow diffusion. This phenomenon has been observed in elliptical point contact conditions in the so-called "keyhole" contact domain [11,21]. The phenomenon described here is not observed along the section 3-3, but along the section 5-5, giving credence to the argument.

3.5 The Extrapolated Film Thickness Equation

A simultaneous quasi-static solution of the EHL problem with multi-body kinematic model renders an unacceptable computation time. The solution for the inertial rigid body kinematics is carried out in a large number of time intervals, typically in the region of 500 steps for each cam revolution. The time requirement for a solution of the EHL problem is typically in the region of 1-2 hours per time step. Therefore, a simultaneous solution is impractical. However, the effect of the lubricated contact dynamics in the multi-body analysis is essential. An appropriate approach is to obtain an extrapolated equation to describe the non-linear characteristics of the EHL conjunction under transient contact dynamic conditions. The solution of the EHL problem under combined entraining and squeeze film motion has been shown to yield such equations that can be used in the dynamic analysis of bearings [22] and gears [15,23]. The same approach is to be adopted here for the case of valve train multi-body dynamics.

To obtain such an equation, 18 simulation runs were undertaken, as indicated in table 3. The following extrapolated film thickness formulae are obtained by regressional analysis:

For the central oil film thickness:

$$h_0^* = 1.67 W^{*0.059} U^{*0.541} G^{*0.421} e^{-96.775 W_s^*} \tag{17}$$

And for the side constriction oil film thickness:

$$h_{sc}^* = 1150 W^{*-0.037} U^{*0.857} G^{*0.406} e^{-138.059 W_s^*} \tag{18}$$

The central oil film thickness equation, conforming closer to the actual numerical results is employed in the contact dynamic analysis to obtain film thickness at all the intervals of time. This formula can be inverted in the dimensioned form to obtain the lubricant film reaction in the form: $W = \Psi(h, \dot{h}, t)$.

4. The Multi-body Model Formulation

There are four parts in the multi-body model, the motion of each of which can be described in terms of a the generalised co-ordinates, q by the Lagrange's equation for constrained systems as:

$$\frac{d}{dt}\left(\frac{\partial K}{\partial \dot{q}}\right) - \frac{\partial K}{\partial q} - F_q + \sum_{k=1}^{n} \lambda_k \frac{\partial C_k}{\partial q} = 0 \tag{19}$$

The generalised co-ordinates are given by: $\{q\} = \{x, y, z, \psi, \theta, \xi\}^T$, where the rotational components are the Euler angles (i.e. body 3-1-3 successive rotations).

The reaction forces in the multi-body system are given by the summation term in equation (19) along each of the generalised co-ordinates. These are introduced by non-linear algebraic scalar functions, C_k. Therefore, the assembly of parts can be represented mathematically in a manner that conforms with the required dynamic functions of the system.

Under dynamic conditions equation (19) provides six equations of motion per part in the valve train system. To illustrate the method of formulation we draw the equations for the case of the flat follower (see figure 7). XYZ is the global fixed frame of reference, attached to any

arbitrary location, whilst x',y',z' is the moving local part frame of reference that is usually attached to the geometric centre or the centre of gravity of the part. This simple two dimensional model of the valve/spring assembly translation motion against the valve guide includes a number of important points, referred to as markers. Constraint functions are formulated by relating the instantaneous position and orientation of these markers $\{q_i\} = f(t)$. The markers chosen in this example are the centre of mass of the follower, m1 and the valve spring attachment location m2, given by the position vectors $\vec{R}_{m2}, \vec{R}_{m1}$ respectively in figure 7. The vector $\vec{r}_{m1m2}$ gives the instantaneous position of marker m1 with respect to marker m2.

The kinetic energy of the valve is given by: $K = \frac{1}{2} m\dot{y}^2$ (20)

Using equation (19), the equation of motion for the valve is obtained as:

$$m(\ddot{y} - g) + k_s + \lambda_2 \frac{\partial C}{\partial y} = 0 \tag{21}$$

The above second order equation can be reduced to a pair of first order equations. This is performed for ease of solution, using step-by-step integration. Therefore:

$$\begin{aligned} &m(\dot{v} - g) + k_s y + \lambda_2 \frac{\partial C}{\partial y} = 0 \\ &v - \dot{y} = 0 \end{aligned} \tag{22}$$

Similarly:

$$\begin{aligned} &m\dot{u} + \lambda_1 \frac{\partial C}{\partial x} = 0 \\ &u - \dot{x} = 0 \end{aligned} \tag{23}$$

The constraint function is formulated as:

$$\vec{C} = \vec{R}_{m1} - (\vec{R}_{m2} - \vec{r}_{m1m2}) = 0 \tag{24}$$

The vectors in equation (24) are known at any time with respect to the fixed global frame of reference as:

$$\begin{aligned} \vec{R}_{m1} &= x_{m1}\hat{i} + y_{m1}\hat{j} \\ \vec{R}_{m2} &= x_{m2}\hat{i} + y_{m2}\hat{j} = const \\ \vec{r}_{m1m2} &= r_x\hat{i} + r_y\hat{j} \end{aligned} \tag{25}$$

The functional dependence of the components r_x, r_y on the Euler angle rotation ψ are taken into account by co-ordinate transformation as:

$$\begin{aligned} r_x &= r_{x'}\cos\psi - r_{y'}\sin\psi \\ r_y &= r_{x'}\sin\psi + r_{y'}\cos\psi \end{aligned} \tag{26}$$

Substituting for all terms into equation (24), we get:

$$\vec{C} = \{x_{m1} - x_{m2} - (r_{x'}\cos\psi - r_{y'}\sin\psi)\}\hat{i} + (y_{m1} - y_{m2} - (r_{x'}\sin\psi + r_{y'}\cos\psi)\}\hat{j} = 0 \quad (27)$$

Therefore:

$$\begin{aligned} \frac{\partial C}{\partial x} &= \vec{C}.\hat{i} = x_{m1} - x_{m2} - (r_{x'}\cos\psi - r_{y'}\sin\psi) \\ \frac{\partial C}{\partial y} &= \vec{C}.\hat{j} = y_{m1} - y_{m2} - (r_{x'}\sin\psi + r_{y'}\cos\psi) \end{aligned} \quad (28)$$

where the symbol "." represents the vector scalar product.

The functional dependence of vector $\vec{r}_{m1m2}$ on angle ψ introduces the Euler momentum equation that is constrained by the function in equation (27) as:

$$\bar{\lambda}\frac{\partial C}{\partial \psi} = \bar{\lambda}.(\hat{k}\wedge\vec{r}_{m1m2}) = \vec{r}\wedge\bar{\lambda}.\hat{k} = \lambda_2 r_y - \lambda_1 r_x \quad (29)$$

where the symbol "^" denotes the vector cross product.

The Euler momentum equation reduced to a pair of first order equations is represented as:

$$\begin{aligned} &I_{zz}\dot{\varpi} + \lambda_2 r_y - \lambda_1 r_x = 0 \\ &\varpi - \dot{\psi} = 0 \end{aligned} \quad (30)$$

Replacing these relations in the equations of motion (22) and (23), the following set of equations for our two dimensional model results:

$$\begin{aligned} &m\dot{u} + \{x_{m1} - x_{m2} - (r_{x'}\cos\psi - r_{y'}\sin\psi)\}\lambda_1 = 0 \\ &m(\dot{v} - g) + k_s y + \{y_{m1} - y_{m2} - (r_{x'}\sin\psi + r_{y'}\cos\psi)\}\lambda_2 = 0 \\ &I_{zz}\dot{\varpi} + \lambda_2(r_{x'}\sin\psi + r_{y'}\cos\psi) - \lambda_1(r_{x'}\cos\psi - r_{y'}\sin\psi) = 0 \\ &u - \dot{x} = 0 \\ &v - \dot{y} = 0 \\ &\varpi - \dot{\psi} = 0 \\ &x_{m1} - x_{m2} - (r_{x'}\cos\psi - r_{y'}\sin\psi) = 0 \\ &y_{m1} - y_{m2} - (r_{x'}\sin\psi + r_{y'}\cos\psi) = 0 \end{aligned} \quad (31)$$

There are 8 unknowns; $u, v, x, y, \varpi, \psi, \lambda_1, \lambda_2$ and 8 equations in (31), in effect allowing the translational motion of the valve along the guide, providing that the contact reaction $W = \Psi(h, \dot{h}, t) = k_s y + \{y_{m1} - y_{m2} - (r_{x'}\sin\psi + r_{y'}\cos\psi)\}\lambda_2$ can be obtained at any step of time. This is provided by the prevailing conditions in the cam/follower contact described below.

In the simplified two dimensional model, the "part" (i.e. the valve/follower) has three degrees of freedom, two of which are restricted by the 2 algebraic constraint functions $\frac{\partial C}{\partial x}$ and $\frac{\partial C}{\partial y}$. Clearly, in the model described in section 2, the valve is represented in three dimensions and in this case 3 further constraint functions exist, as well as the equations of motion relating to θ and ξ in the Euler body 3-1-3 frame of reference.

The prevailing conditions in the contact of cam-follower can be imposed by series of constraint functions. For the three dimensional model, described in section 2, these relate to the in-plane rotation of the cam, constraining the out of plane rotations about X and Y global axes (two constraints), and constraining the contact line on the follower to coincide with the cam profile at all times (i.e. constraining the out of plane excursion of the follower- one constraint). The final constraint corresponds to no slip condition (i.e. no relative velocity between the cam and follower contact points). These four constraint functions are required for the three dimensional model, as shown in table 2. In the case of the simplified two dimensional example, these conditions translate into the determination of follower velocity as a function of cam profile. This velocity is the derivative of the of the follower's instantaneous position from the cam centre which can also be represented as the product of the cam speed and the perpendicular distance from the cam centre to the instantaneous point of contact (see figure 8). Thus:

$$\dot{y} = \frac{dR}{dt} = l\Omega \tag{32}$$

This motion constraint, therefore, renders our multi-body model as a kinematic system.

5.0 Cam/follower contact stress analysis

The failure of cam/follower friction pair occurs either as a result of wear of surfaces caused by depletion of the lubricant film or by fatigue spalling of the contacting bodies through sub-surface stresses. A simplified solution for sub-surface stresses can be obtained at instances of high load through the cam cycle. In such a simplified solution two dimensional sub-surface stresses can be obtained along the line of contact normal and in the bulk of the material, both for the cam and the follower. In the simplified solution the maximum EHD pressure profile through the primary peak can be approximated by a parabolic pressure distribution. This assumption ignores the stress field set up by the secondary pressure spike, which can be significant as suggested by references [11,12,24]. The assumption of the elliptical pressure profile, however, is found to be reasonable as it closely follows the ellipsoidal Hertzian pressures. This approach has been highlighted by Johns-Rahnejat [24], and is employed here.

The dimensions of the concentrated finite line contact area between the cam and the follower is small compared to the principal radii of curvature of the contact. Therefore, the elastic bodies in contact can be regarded as elastic half-spaces. It has been shown in reference [24] that for a parabolic pressure distribution, acting upon an elastic half-space under plane strain condition, the two dimensional sub-surface stresses at a distance z below the surface are:

$$\bar{\sigma}_{\bar{x}} = -2\bar{z}\int_{-1}^{+1} (\bar{x} - \bar{x}_1)^2 (1 - \bar{x}_1^2).\{(\bar{x} - \bar{x}_1)^2 + \bar{z}^2\}^{-2}.d\bar{x}_1 \tag{33}$$

$$\overline{\sigma}_{\bar{z}} = -2\bar{z}^3 \int_{-1}^{+1} (1-\bar{x}_1^2).\{(\bar{x}-\bar{x}_1)^2 + \bar{z}^2\}^{-2}.d\bar{x}_1 \tag{34}$$

$$\overline{\tau}_{\bar{x}\bar{z}} = 2\bar{z}^2 \int_{-1}^{+1} (\bar{x}-\bar{x}_1)(1-\bar{x}_1^2).\{(\bar{x}-\bar{x}_1)^2 + \bar{z}^2\}^{-2}.d\bar{x}_1 \tag{35}$$

where the non-dimensional groups are:

$$\bar{x} = x/b, \bar{z} = z/b, \bar{x}_1 = x_1/b, d\bar{x}_1 = dx_1/b, \overline{\sigma} = (\pi\sigma/P_m) \tag{36}$$

When the stresses along the $\bar{z}$ axis are considered, $\bar{x} = 0$:

$$\overline{\sigma}_{\bar{x}}(0,\bar{z}) = 6\bar{z} - 2(1+3\bar{z}^2)\tan^{-1}(1/\bar{z}) \tag{37}$$

$$\overline{\sigma}_{\bar{z}} = (0,\bar{z}) = -2\bar{z} + 2(\bar{z}^2 - 1)\tan^{-1}(1/\bar{z}) \tag{38}$$

$$\overline{\tau}_{\bar{x}\bar{z}}(0,\bar{z}) = 0 \tag{39}$$

The above stress distribution along the line of contact normal applies to the maximum sub-surface stress field for the flat follower. Assuming the cam to be represented as a disk shaped object of variable radius, Johns-Rahnejat [24] has shown that the stress field along the contact normal will be approximately the same as that of the follower, but would be different in other sub-surface locations.

The maximum shear stress which is primarily responsible for the fatigue failure of the contacting members occurs along the line of contact normal, and below the surface at a distance of z=0.78b with a magnitude of $0.3P_m$. The value of maximum shear stress is obtained as half the difference of the above calculated principal stresses.

6.0 Results of Multi-body Dynamic Model

The main task in the design of cam/follower friction pair is to ensure coherent lubrication by providing a sufficient oil film thickness guarding against wear, whilst ensuring contact loads that do not exceed the fatigue strength limits.

The problem is that conditions that yield low loads and thus reduced Hertzian pressures do not necessarily render optimal lubrication conditions. This problem was first discovered by Müller [25], who showed that a cam with higher radius of curvature, enjoying lower maximum Hertzian stresses can yield lower lubricant film thicknesses. This finding is now generally accepted and has been corroborated by both experimental and theoretical investigations [5,7,26,27]. Quasi-static EHL solutions have indicated higher lubricant film thicknesses at high Hertzian stresses than those generated by other prevalent regimes of lubrication at low contact loads [7,8,26]. The rather complex relationship between dynamic contact loads and lubrication can only be studied in an integrated solution of valve train kinematics and lubricated contact dynamics of cam/follower.

The solution provided in this paper, therefore, integrates EHL of finite line contact of cam and follower in the kinematics of the valve train system.

In this study, we have employed a cycloidal cam profile, typical of a mid-height camshaft and a flat follower arrangement. The cycloidal cam in such an arrangement can have a rather broadened flat nose in order to follow the required constant lift profile as shown in figure 9. The cycloidal curve is used often as a basis of designing cams, especially for high speed applications. It yields low noise, vibration and wear characteristics. Furthermore, there are no abrupt changes in associated valve train accelerations and for a given rise and time the acceleration is somewhat higher than that of many other types of cam. The trend in the development of modern valve train systems is towards faster acting systems with lower component masses. Therefore, modified cycloidal curves can be employed to produce the desired valve accelerations and owing to high accelerations the instances of zero entraining velocities in the contacting region are short lived, resulting in rapid lubricant replenishment. However, high values of acceleration and decelerations with cycloidal cams can result in high inertial forces and must be kept under control with correspondingly stiff valve springs. Therefore, valve train design problems are somewhat accentuated when cycloidal cams are employed. Precisely because of this reason, such a cam profile is employed in this study to illustrate the cam/follower design problems. Also that detailed kinematic, lubrication and structural integrity study of cycloidal cams have not been reported in literature to the same extent as the more conventional higher polynomial automotive cams. In addition cycloidal cams have been used extensively in other high speed machinery applications.

The kinematic relations for a flat follower is relatively simple. This allows for the differentiation of the valve lift over the cam angle which yields the velocity and the acceleration profiles (also shown in figure 9). Note should be taken that for an arrangement of a cycloidal cam and a flat follower the follower acceleration has a sharp spike at the contact with the cam nose. This is because with the cycloidal curve, the follower acceleration is symmetrical about the cam half cycle. The advantage of this is that the acceleration variation is continuous [28,29]. The disadvantage of this is seen in lubrication conditions within the vicinity and prior to the cam nose contact as would be discussed later. This disadvantage is alleviated due to fast contact transit time at high speeds (as previously discussed). Therefore, at low speed revolutions the lubrication performance of this type of cam can be poor. The follower velocity profile exhibits a point of inflexion relating to the acceleration reversal at the cam nose contact. These characteristics of the arrangement employed here have been observed experimentally be Fessler and Ham [27].

Empirical formulae for lubricant film thickness for EHD line contact conditions have been obtained by various researchers [9,10,17,18,30,31]. These formulae corrolate with the experimentally measured film reported by others [5,27], except for regions where the speed of entraining motion is zero or subject to fast changes, indicating inlet boundry reversals. In these regions the squeeze film effect is found to be a significant contributory factor in lubrication film retention [5,7,8,27]. In the regions of zero entrainment velocity, the squeeze effect support the loads and prevents surface to surface contact. It should also be noted that the time window in these regions is very short indeed and the entraining flow is rapidly replenished [8].

In the current study, finite line EHD contact under pure entraining motion is considered and the extrapolated equation for entraining motion is included in the kinematic model. Figure 10(a) shows the variation of entraining velocity during a cam cycle. The corresponding lubricant film thickness and the maximum Hertzian pressure are shown in figures 10(b) and 10(c). The cam nose location is designated to be at 180° , with the flank and nose actions occurring from 90° to 270°. It should be noted that the entraining velocity crosses the zero value at four locations (see figure 10(a)). With the polynomial automotive cams there are only two points of zero entrainment, usually occurring at angles ±36° - ±46° from the cam nose. In cycloidal cams, however, due to the somewhat broadened nose profile a high value of entraining velocity is

achieved there, thus causing zero entraining velocities at ±15° as well as ±51° as shown in figure 10(a). The corresponding lubricant film thickness is, therefore, at a minimum value in these regions. This is found to be 0.03μm. this is a very small film thickness that in practice is supplemented by the squeeze film effect (not included in our present EHL formula) and rapid replenishment in a short interval of time. The lubricant film at the nose, however, is much larger as the speed of entraining motion there is in excess of 4m/sec, giving a film thickness just below 1μm. The lubricant film thickness is much larger in the other regions, but never in excess of 1.3μm for this analysis. The conditions in these analysis are quite similar to those reported by Dowson et al [7], except that in their case a fourth order polynomial cam is employed. In their analysis the film thickness reaches a minimum value at two locations ±37° to the cam nose (as it would be in the case of a polynomial cam) with a film thickness of approximately 0.08μm, retained entirely by the squeeze film effect.

Figure 10(c) shows the maximum Hertzian pressure reaching a value of 325MPa at locations ±62° to the cam nose. The pressure subsequently drops to a value of approximately 180MPa at the cam nose. In-fact the Hertzian pressure drops as the instantaneous cam radius (the relative radius of contact increases). This can be observed from figures 10(c) and 10(d). The contact width required for the evaluation of finite line EHD conditions, the corresponding contact elastic deflection and contact load are shown in figures in 11(a), 11(b) and 11(c) respectively. It is observed that an increasing contact load corresponds to an increase in elastic deflection. Furthermore, the contact width used in the three dimensional solution of the EHD pressures described above also increases with contact load.

The sub-surface stress field along the line of contact normal is obtained at positions of maximum Hertzian pressures during the cam cycle indicated in figure 10(c), at the cam nose and at ±62° to it. These are shown in figures 12(a) and 12(b) respectively. The maximum direct stress in the cam cycle is approximately 325 MPa as shown in figure 12(b) at the surface for the normal principal stress which is within the fatigue limit of the cam, having a compressive yield strength of $\sigma_{limit} = 400 - 500MPa$. The maximum shear stress occurs below the contact in figure 12(b), having a value of 96 MPa, which is below $\frac{1}{2}\sigma_{limit} = 200 - 250MPa$, as required by Tresca criterion.

7.0 Conclusion

The analysis indicates that valve train kinematics, incorporating tribo-contact dynamics of cam and flat follower is a complex problem that profoundly affects the performance of IC engines. Traditional methods of dealing with lubrication, valve train kinematics, and contacting bodies structural integrity in isolation are not suitable for design analysis of modern valve train systems. The approach highlighted in this paper is seen to contribute to modern engine valve train development, where more lighter components are increasingly subjected to higher duty cycles.

Acknowledgements

The authors would like to express their gratitude to Mr. Suresh Gupta of Mechanical Dynamics International (MDI) UK Ltd for his support and encouragement.

NOMENCLATURE

b : Contact half-width
C : Constraint function
D : Instantaneous cam diameter
e : Exponentiation
E : Modulus of Elasticity
F_q : Vector of generalised forces
g : Gravitational accceleration
G* : $E\alpha$
h : Lubricant film thickness
$\dot{h}$: Squeeze film velocity
h* : Dimensionless lubricant film thickness
I ; Moment of inertia
i, j, k : Unit vectors in Cartesian frame of reference
k_s : Valve spring rate
K : Kinetic energy
l : Distance from the cam centre to the instantaneous centre of curvature
L : Contact length
m : mass
n : Number of constraints
p : Hertzian or EHL pressure
p* : p/E
p_r : Cam contact profile
{q} : Generalised co-ordinates
q, q* : Reduced hydrodynamic pressure
R : Instantaneous reduced radius of the counterformal contact
$\vec{R}$: Position vector with respect to global frame of reference
$\vec{r}$: Position vector with respect to local frame of reference
s : Follower lift
t : Time
u : Entraining velocity
U* : $U\eta / ER$
W : Contact load
W* : W/ERL
w_s : Squeeze velocity
w_s* : Squeeze-roll speed ratio
X,Y,Z : Global Cartesian frame of reference
x,y,z : Local Cartesian frame of reference
z : Depth beneath the cam surface
α : Lubricant piezo-viscosity index
λ : Lagrange multiplier
δ : Contact deflection
ρ : Lubricant density
η : Lubricant dynamic viscosity
υ : Poisson's ratio
ψ, θ, ξ : Euler angles
Ω : Cam speed
σ : Direct compressive sub-surface stress
τ : Sub-surface shear stress

REFERENCES

1. Taylor C.M., "Fluid film lubrication in automobile valve trains", Proc. Instn. Mech. Engrs., Part J: J. Engng. trib.,Vol.208, pp.221-234, 1994
2. Ciulli E., "A review of internal combustion losses part1 specific studies on the motions of pistons, valves and bearings", Proc. Instn. Mech. Engrs., Part D: J. Auto.Engng.,Vol.206, pp.223-226, 1992
3. Eichhorn U. and Schonfeld H., "The valve train of internal combustion engines as a source of vibrations-experimental results and methods of calculations", Proc. XXIII FISITA Congress, Torino (Italy), pp.389-395, May 1990
4. Rahnejat H., Multibody Dynamics: Vehicles, machines and mechanisms, MEP Press, inprint.
5. Hamilton M., "The Hydrodynamics of a cam follower", Trib. Int., pp.113-119, June 1980
6. Dyson A., "Kinematics and wear patterns of cam and finger follower automotive valve gear", Trib. Int. pp.121-132, June 1980
7. Dowson D., Taylor C.M. and Zhu G., "A transient elastohydrodynamic lubrication analysis of a cam and follower", J. Phys. D: Appl. Phys., Vol.25,.pp.313-320, 1992
8. Xiaolan Ai., Haiqing Yu., "A numerical analysis for the transient EHL process of a cam-tappet pair in I.C. Engine", Trans. ASME, J. Trib., Vol.111, pp.413-417, July 1989
9. Rahnejat H., Influence of vibration on the oil film in concentrated contacts, PhD. Thesis, Imperial college of Science and Technology, 1984
10. Mostofi A. and Gohar R., "Oil film thickness and pressure distribution in elastohydrodynamic point contacts", J. Mech. Eng. Sci., Vol.24(4), pp.173-182, 1982
11. Johns-Rahnejat P.M. and Gohar R., "Point contact elasto-hydrodynamic pressure distribution and sub-surface stress field", in Rahnejat H. and Walley R. (Eds.) Multibodi dynamics: Monitoring and simulation techniques, MEP Press, pp.161-178,1997
12. Houpert L., Ioannides E., Kuypers J.C. and Tripp J., "The effect of the EHD pressure spike on rolling bearing fatigue", Trans. ASME., J. Trib.,Vol.108, 1986
13. Czyzewsky T., "Changes in the stress field in the elastohydrodynamic contact zone due to some operating factors and their role in the rolling contact fatigue of cylindrical surfaces", Wear, Vol.31, 1975
14. Johns-Rahnejat P.M., The design of cylindrical rollers for use in shaft and bearing systems, MSc. Thesis, Imperial college of Science and Technology, 1978
15. Rahnejat H., "Computational modelling of problems in contact dynamics", Engng. Anal.,Vol.2(4),pp.192-197, 1985
16. Johns P.M. and Gohar R., "Roller bearings under radial and eccentric loads", Trib. Int., pp.131-136, June 1981
17. Mostofi A., Oil film thickness and pressure distribution in elastohydrodynamic elliptical contacts, PhD. Thesis, Imperial college of Science and Technology, 1981
18. Dowson D.and Higginson G.R., Elasto-hydrodynamic lubrication, Pergamon Press, SI Edition, 1977
19. Jalili-Vahid D., Rahnejat H. and Jin Z.M., "Elasto-hydrodynamic lubrication of point contact under combined rolling and squeeze film motion", in Rahnejat H. and Walley R. (Eds.) Multibodi dynamics: Monitoring and simulation techniques, MEP Press, pp.179-186,1997
20. Rahnejat H. and Gohar R., "Design of profiled taper roller bearings", Trib. Int., pp.269-275, December 1979
21. Johns-Rahnejat P.M. and Gohar R., "Measuring contact pressure distributions under elasto-hydrodynamic point contact", TriboTest, Vol.1(1), 1994
22. Rahnejat H. and Gohar R., " The vibrations of radial ball bearings", Proc. Instn. Mech. Engrs., Vol.199(C3), pp.181-193, 1985

23. Mehdigoli H., Rahnejat H. and Gohar R., "Vibration response of wavy surfaced disc in elasto-hydrodynamic rolling contact", Wear, Vol.139, pp.1-15, 1990
24. Johns-Rahnejat P.M., Pressure and stress distribution under elast-hydrodynamic point contacts, PhD. Thesis, Imperial college of Science and Technology, 1988
25. Muller R., 1996 Motor Tech. Z. (Stuttgart) 27-58
26. Xuesong M. and Youbai X., "A numerical analysis of the nonsteady EHL process in high-speed rotating engine cam/tappet pairs", Trans. ASME., J. Trib.,Vol.118, pp.637-643, July 1996
27. Fessler H. and Ham R., "Lubrication and stress analysis as a basis for camshaft optimisation", Proc. XXIII FISITA Congress, Torino (Italy), pp.565-579, May 1990
28. Jensen P., Cam Design and Manufacture, Ind. Press. New York, 1965
29. Reeve J., Cams for Industry, MEP Press, 1997
30. Chittenden R.J., Dowson D., Dunn J.F. and Taylor C.M., "A theoretical analysis of the isothermal elasto-hydrodynamic lubrication of concentrated contacts-part II: general case, with lubrication entrainment along either principal axis of the Hertzian contact ellipse or at some intermediate angle", Proc. Roy. Soc. Lond., A, Vol.397, 1985
31. Hamrock B.J and Dowson D., "Isothermal elasto-hydrodynamic lubrication of point contacts", trans. ASME., J. Lubn. Tech., Vol.99, pp.264-276, 1977

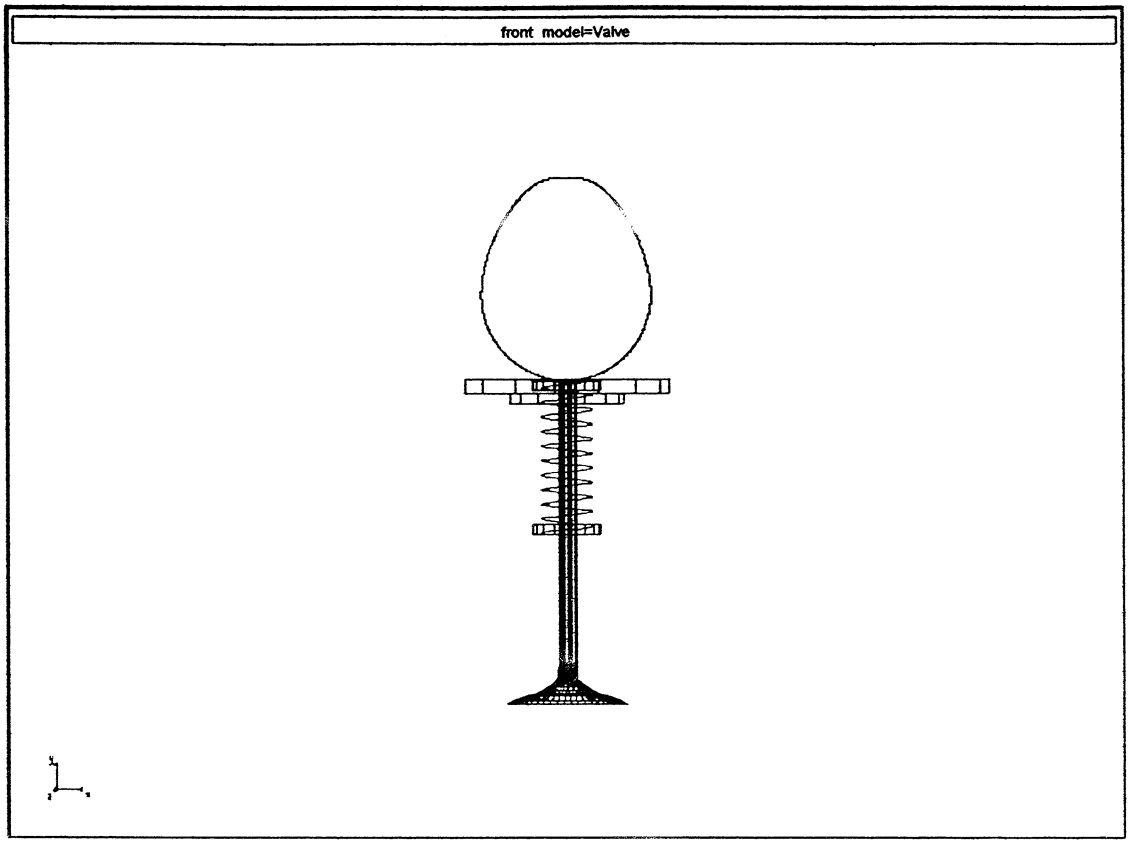

Figure 1. A schematic representation of the kinematic model

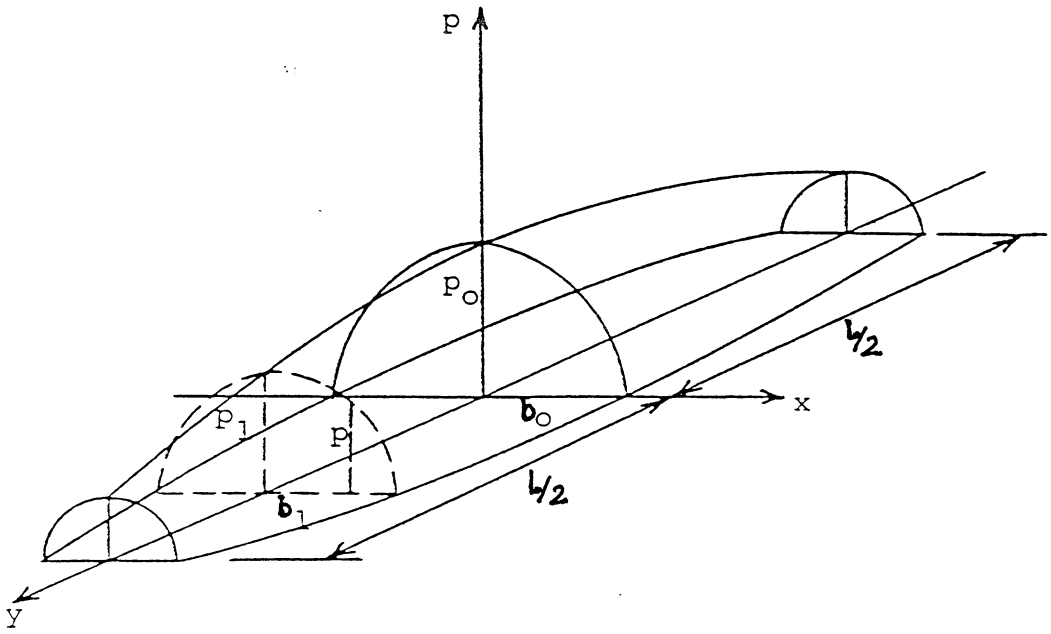

Figure 2

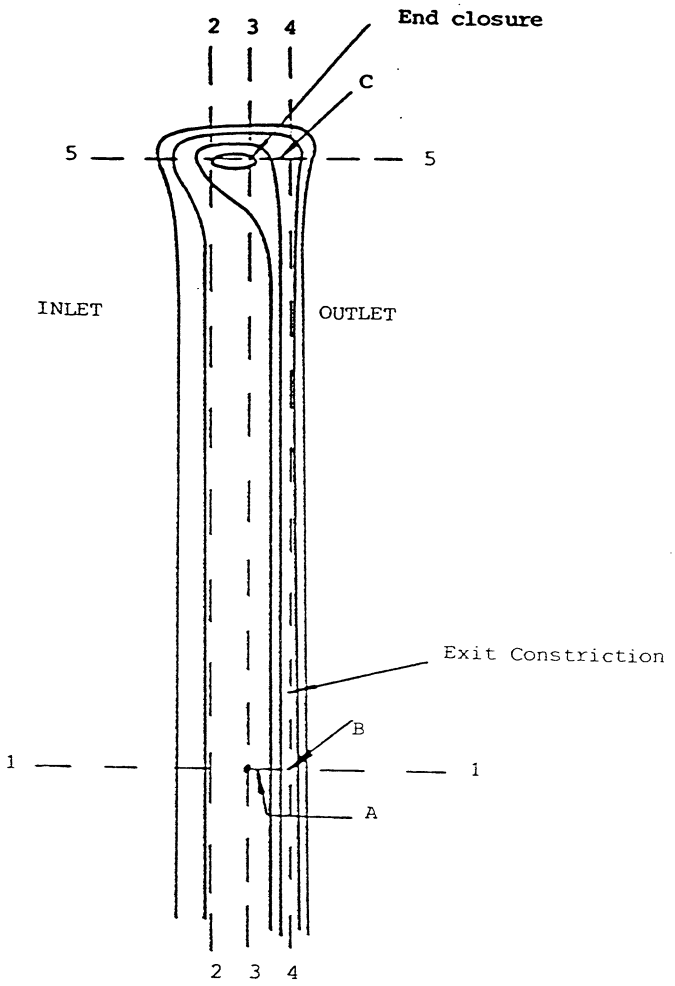
2 3 4
End closure
C
5
5
INLET
OUTLET
Exit Constriction
B
1
1
A
2 3 4

Figure 3

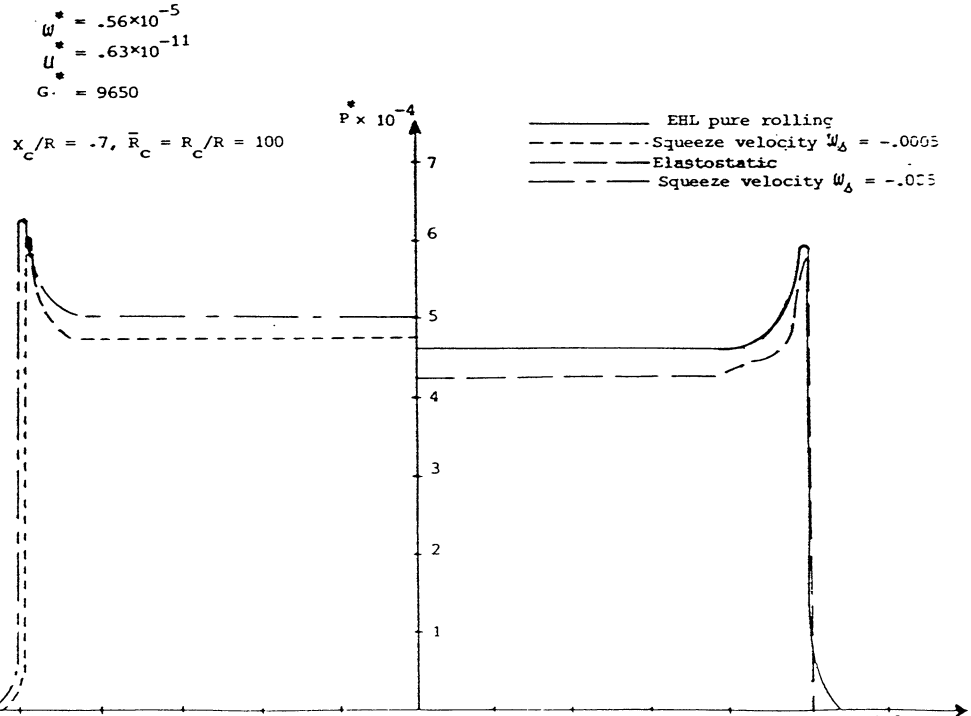
$\omega^* = .56\times10^{-5}$
$u^* = .63\times10^{-11}$
$G^* = 9650$
$X_c/R = .7$, $\bar{R}_c = R_c/R = 100$
$P^* \times 10^{-4}$
EHL pure rolling
Squeeze velocity $\dot{w}_\delta = -.0005$
Elastostatic
Squeeze velocity $\dot{w}_\delta = -.005$
7
6
5
4
3
2
1

$W^* = .56\times10^{-5}$

$U^* = .63\times10^{-11}$

$G^* = 9650$

$X_c/R = .7$

$\bar{R}_c = 100$

Note: for a constant load a thicker film is formed at higher value of W_δ.

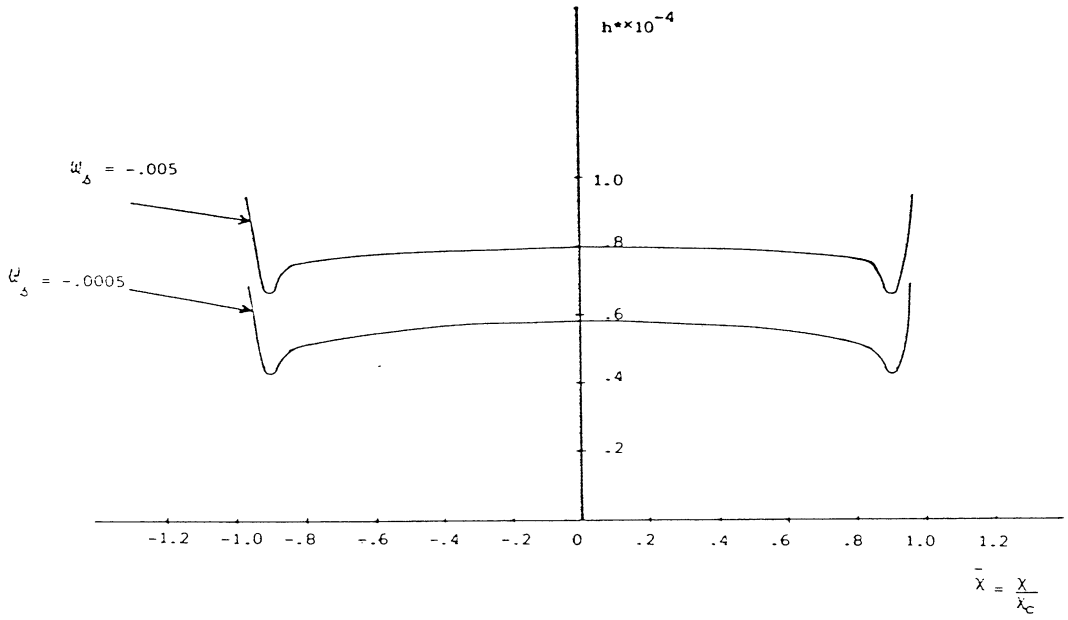

Figure 4B

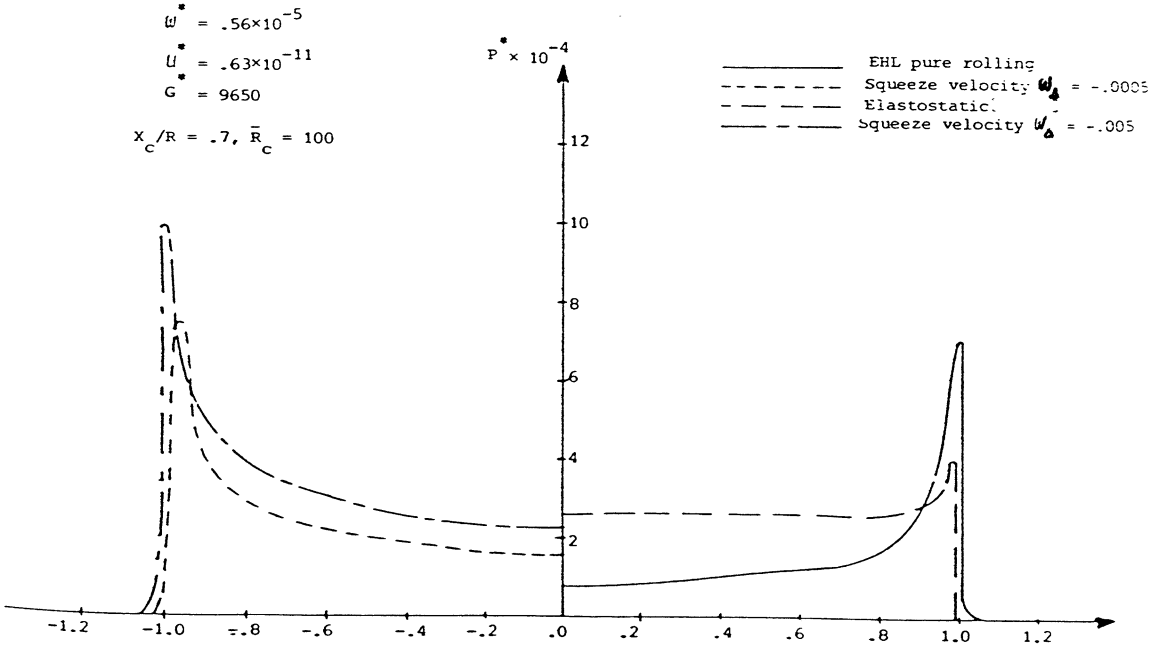

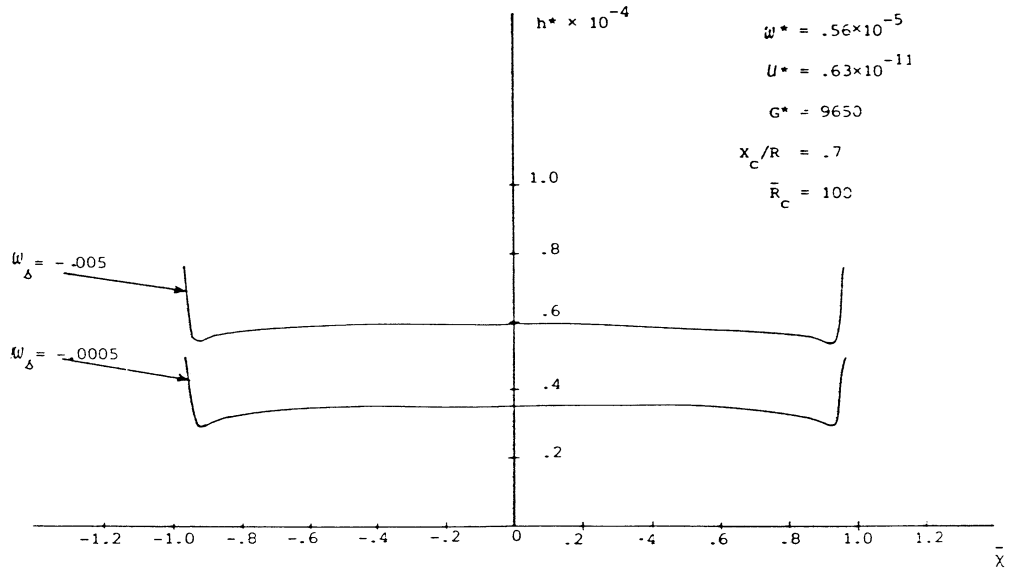

Figure 6

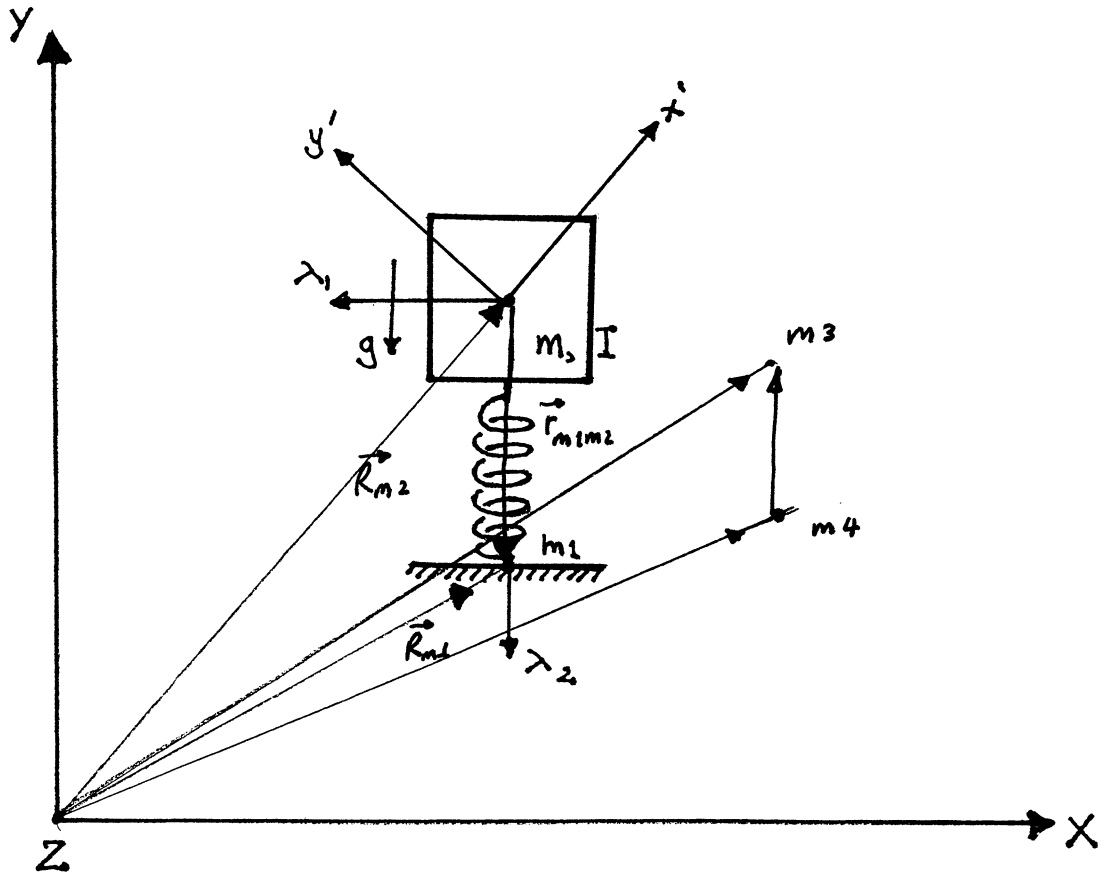

Figure 7

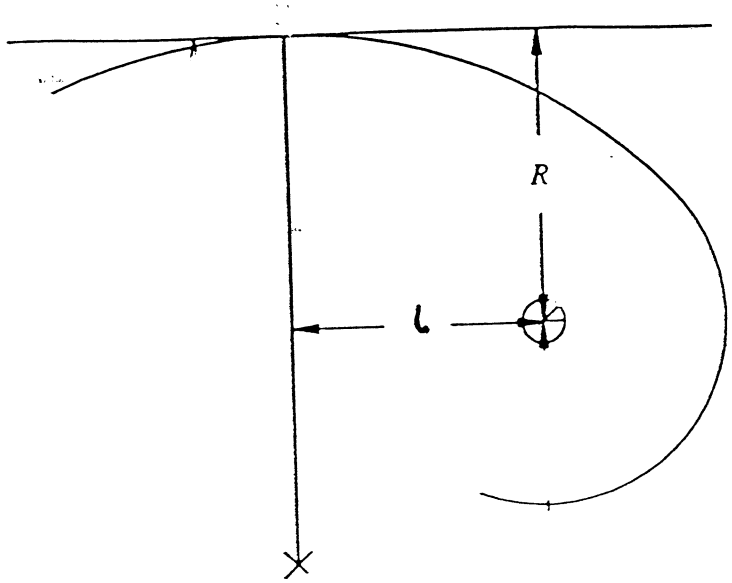

Figure 8

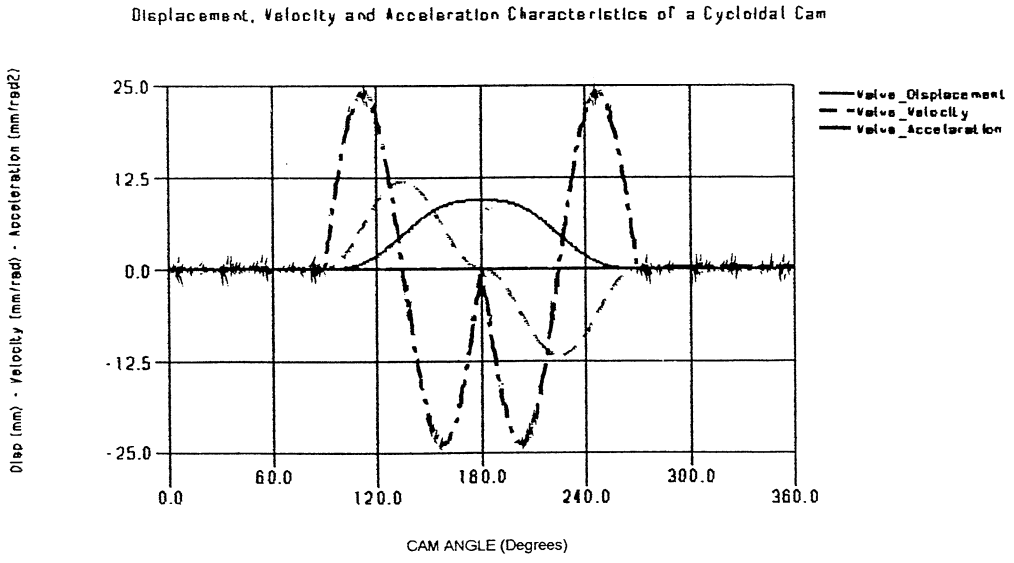

Figure 9

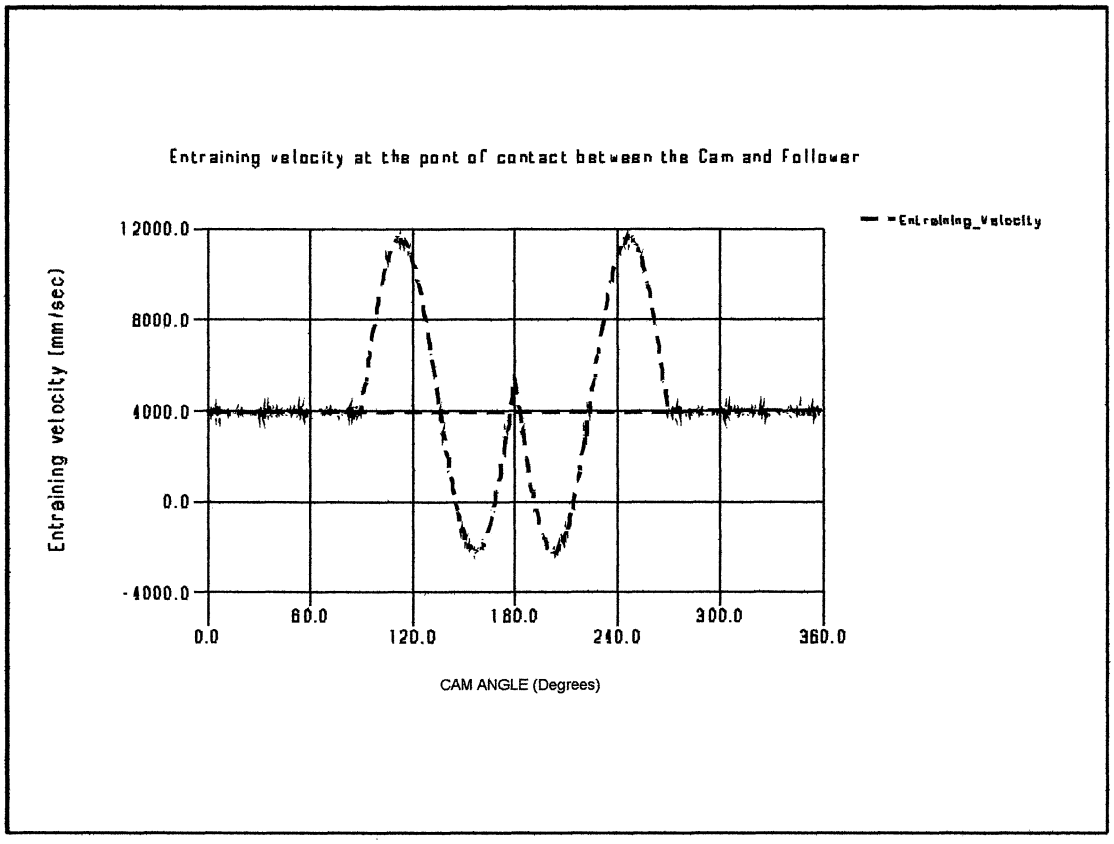

Figure 10(a)

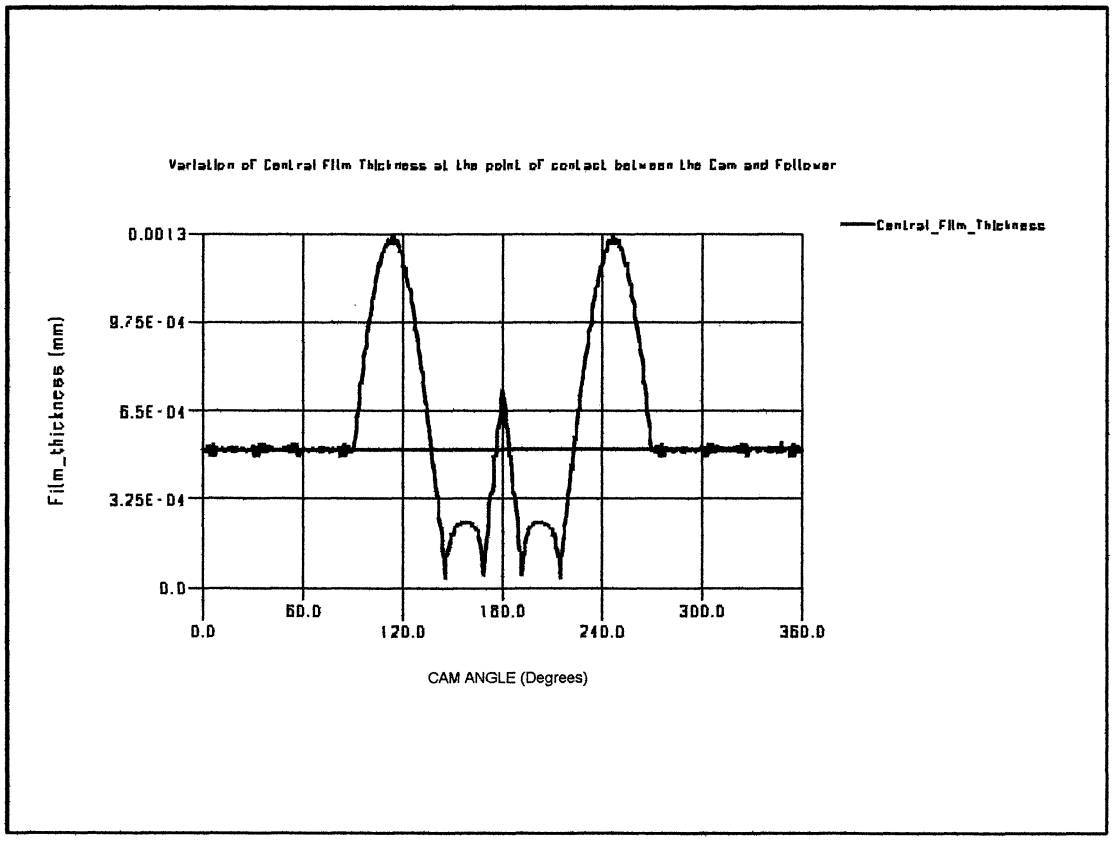

Figure 10(b)

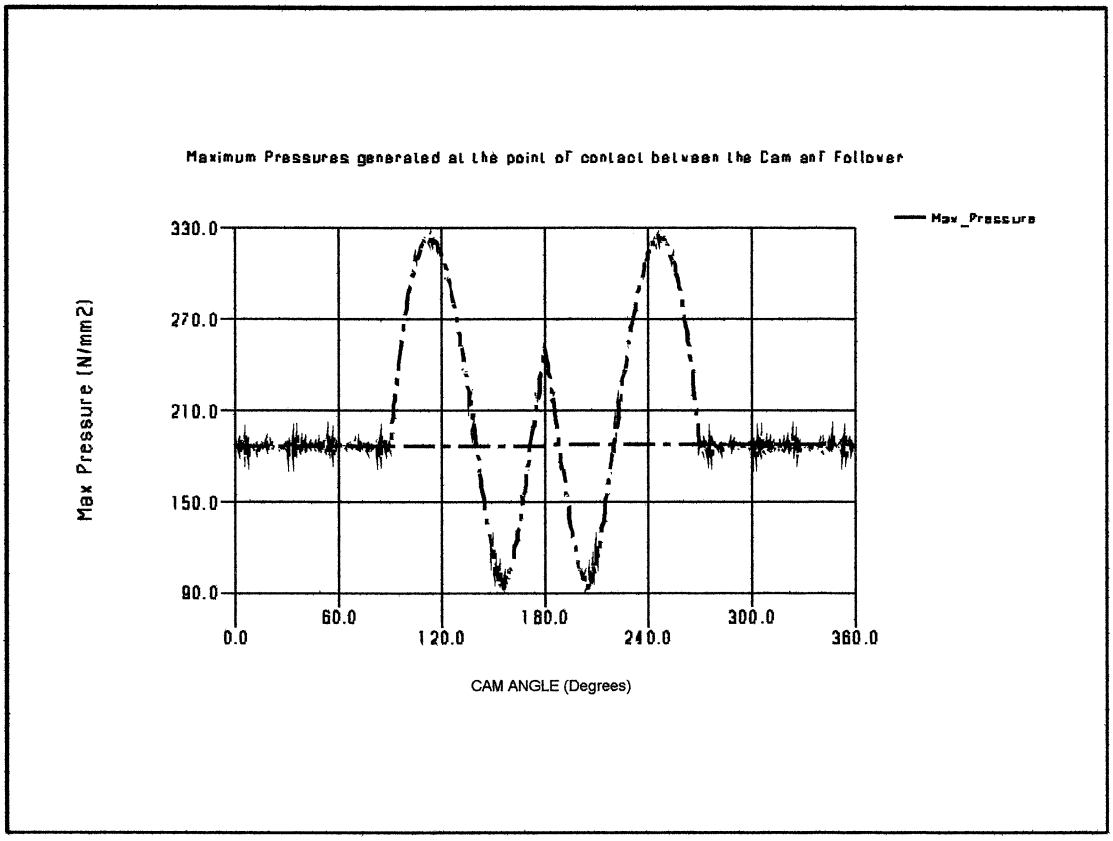

Figure 10(c)

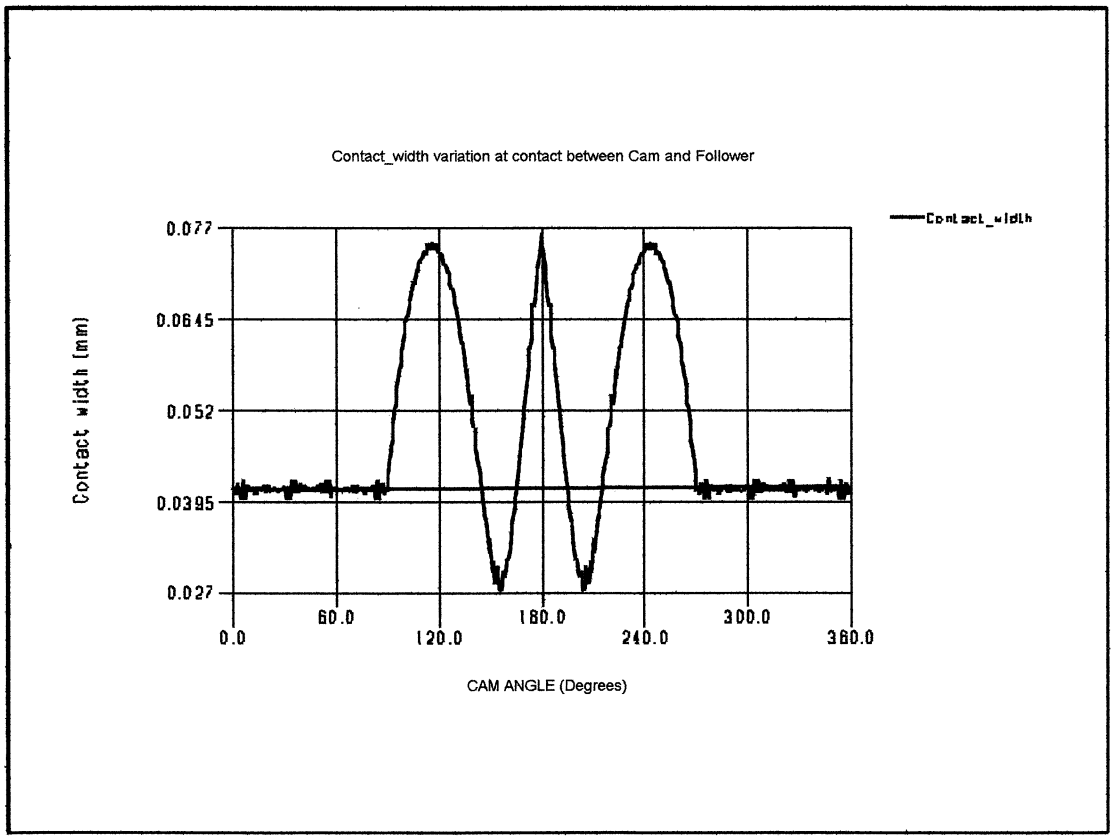

Figure 11(a)

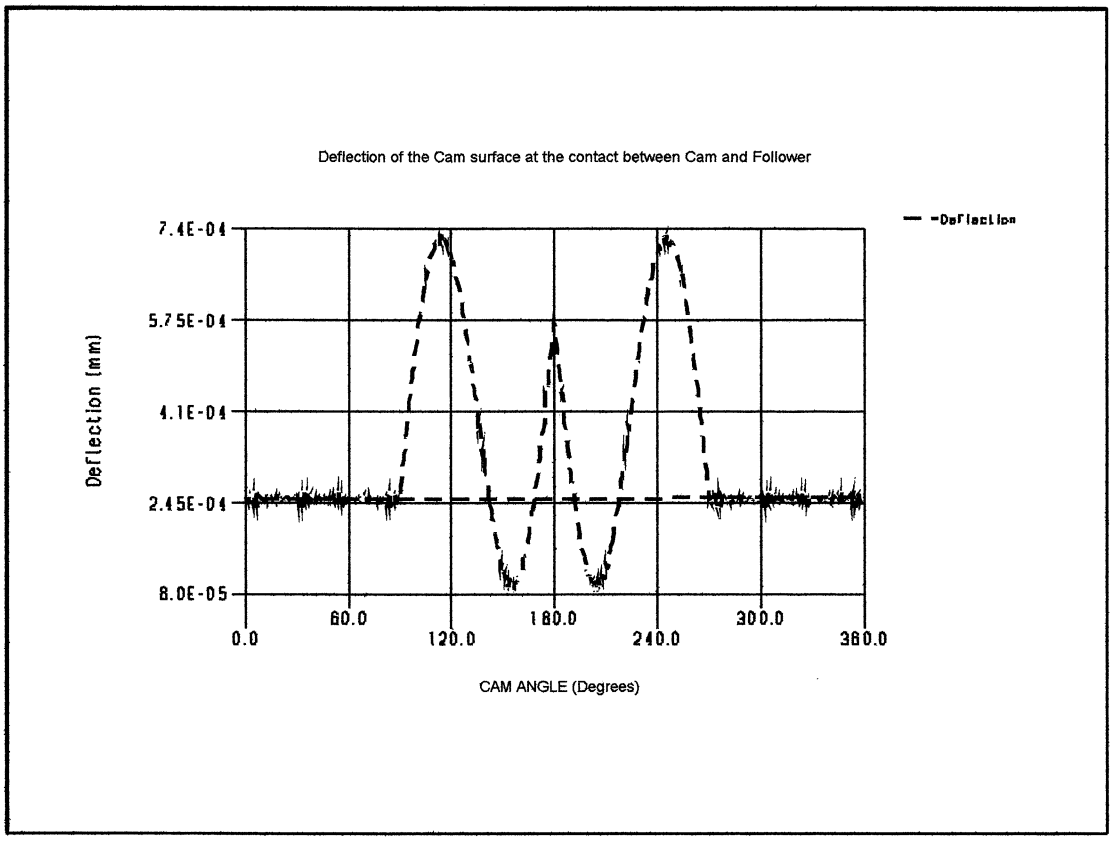

Figure 11(b)

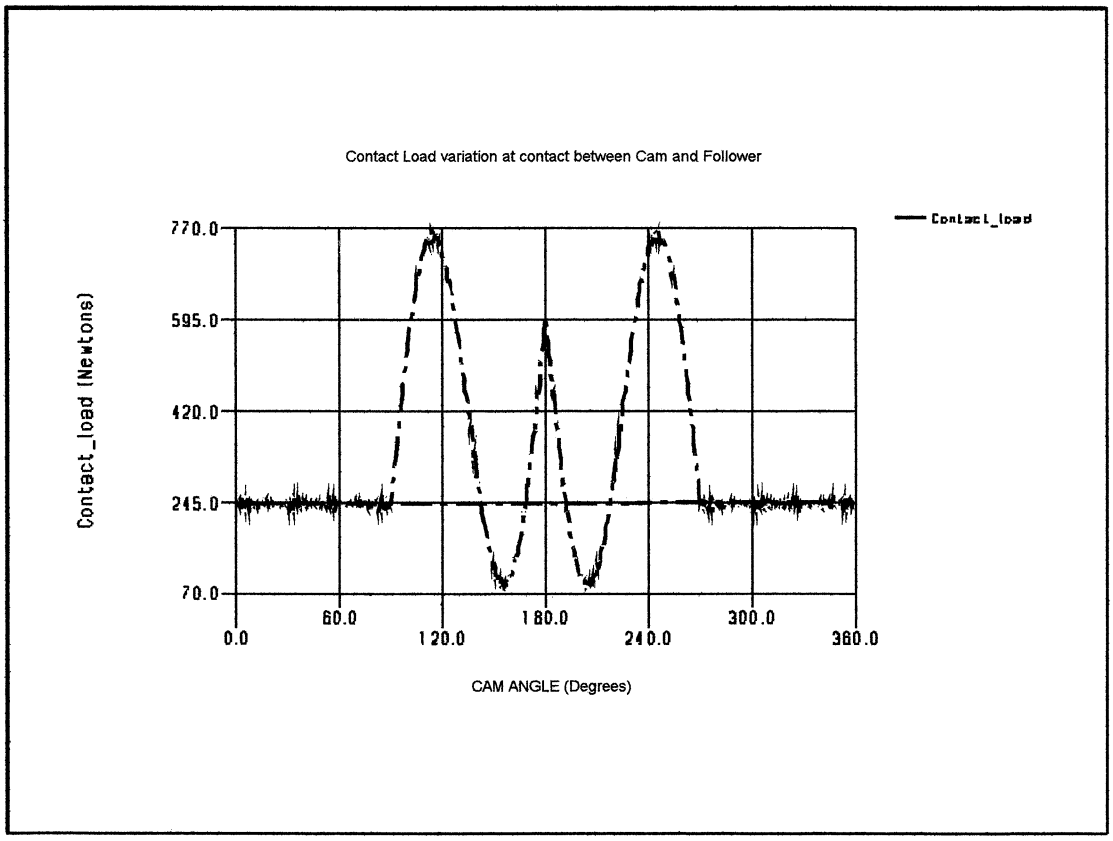

Figure 11(c)

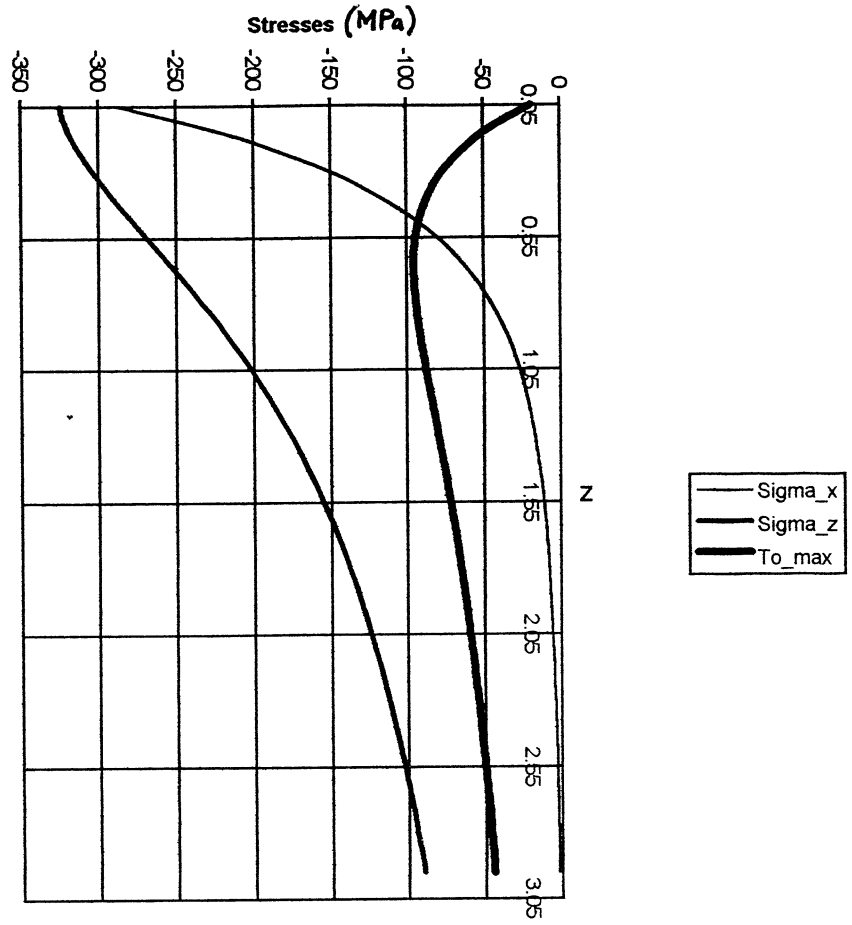

Figure 12A Sub-surface stress field along the line of contact normal at print of Maximum Hertzian Pressure

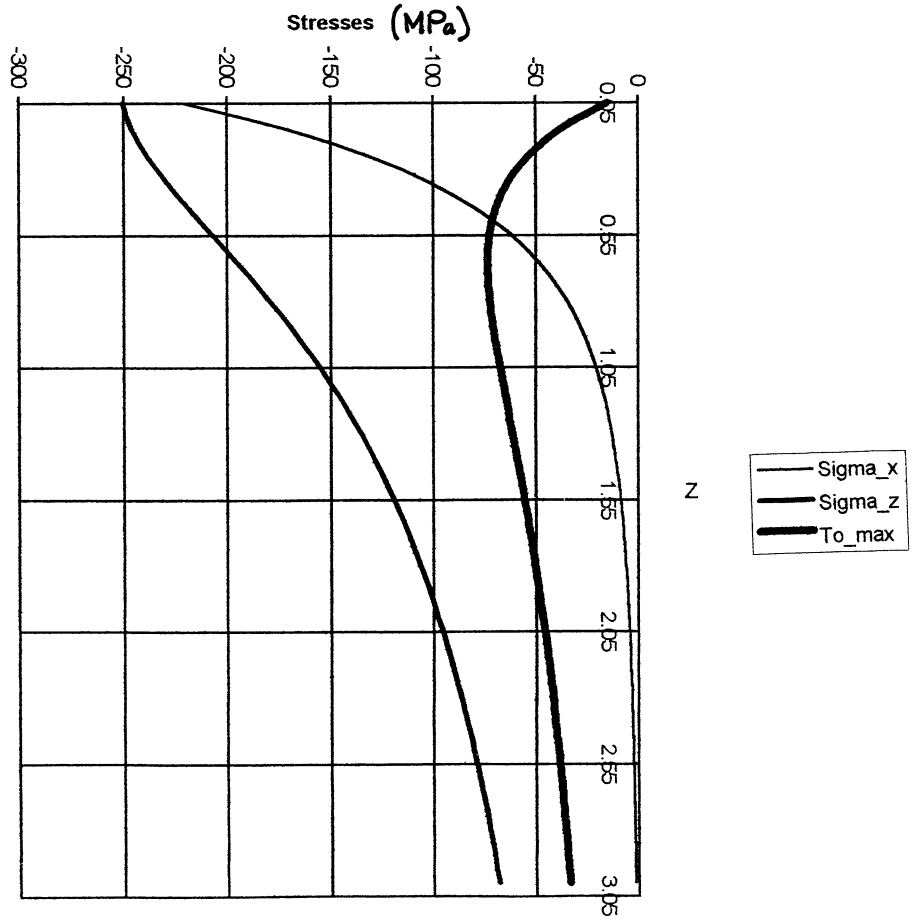

Figure 12B Sub-surface stress field along the line

Rigid Part Name	Mass (Kg)
Camshaft	0.193
Camlobe	0.275
Relainer	0.045
Valve	0.157
Ground	∞

Table 1

Part 1_Name	Part 2_Name	Constraint	Global Coordinate Location
Camshaft	Ground	Translational (locked)	0.0, 0.0, 5.0
Camlobe	Camshaft	Cylindrical (Motion Specified)	0.0, 0.0, 5.0
Camlobe	Retainer	Curve to Curve	-
Retainer	Valve	Fixed	0.0, -25.0, 5.0
Valve	Ground	Translational	0.0, -70.0, 5.0

Table 2

Grouping	Range	Number of Values Taken	Maximum Difference Between Regressed and Numerical Results as a Percentage Difference	
			For $h^*_{\delta c}$	For h^*_0
G^*	5700 → 9650	4	7.9	7.6
w^*_δ	-0.005 → 0	5	32.6	5.8
W^*	$0.34 \times 10^{-6} \rightarrow 0.56 \times 10^{-5}$	6	13.1	4.7
U^*	$0.63 \times 10^{-11} \rightarrow 3.3 \times 10^{-11}$	8	12.5	2.5

Table 3